IEEE Photonics Journal
An IEEE Photonics Society Publication

Open Access

Mid-Infrared Spectral Compression of Soliton Pulse in an Adiabatically Suspended Silicon Waveguide Taper

Volume 11, Number 4, August 2019

Yujun Cheng
Jinhui Yuan, *Senior Member, IEEE*
Chao Mei
Feng Li
Binbin Yan
Xian Zhou
Qiang Wu
Kuiru Wang
Xinzhu Sang
Keping Long, *Senior Member, IEEE*

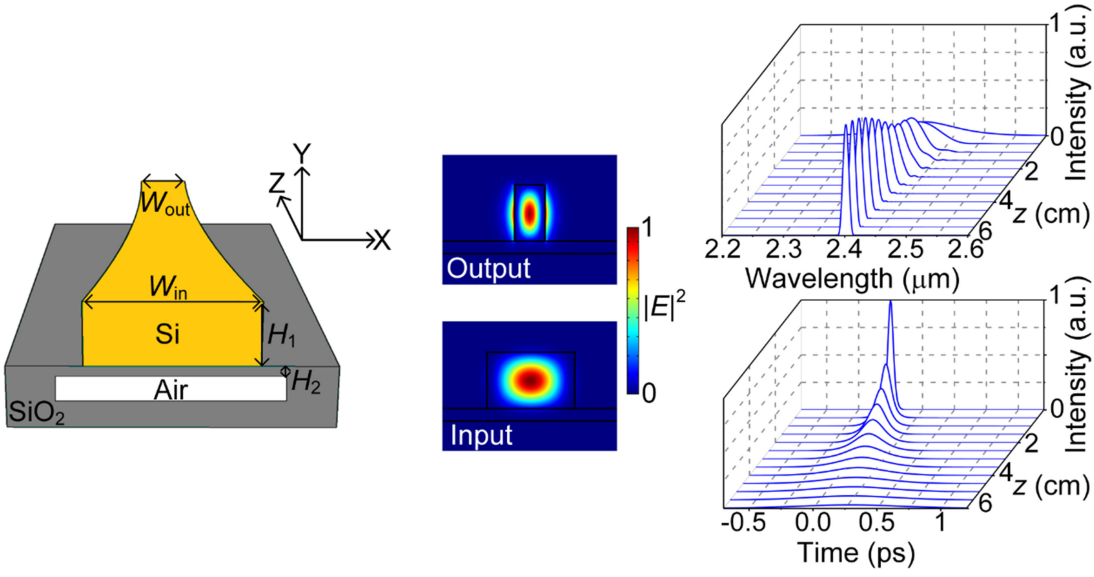

DOI: 10.1109/JPHOT.2019.2927392

IEEE photonics SOCIETY
IEEE

Mid-Infrared Spectral Compression of Soliton Pulse in an Adiabatically Suspended Silicon Waveguide Taper

Yujun Cheng,[1] **Jinhui Yuan**,[1,2] ***Senior Member, IEEE***,
Chao Mei,[1] **Feng Li**,[2] **Binbin Yan**,[1] **Xian Zhou**,[3] **Qiang Wu**,[4]
Kuiru Wang,[1] **Xinzhu Sang**,[1] **and Keping Long**,[3] ***Senior Member, IEEE***

[1]State Key Laboratory of Information Photonics and Optical Communications, Beijing University of Posts and Telecommunications, Beijing 100876, China
[2]Department of Electronic and Information Engineering, Photonics Research Centre, The Hong Kong Polytechnic University, Hong Kong SAR
[3]School of Computer and Communication Engineering, University of Science and Technology Beijing, Beijing 100083, China
[4]Department of Physics and Electrical Engineering, Northumbria University, Newcastle upon Tyne NE1 8ST, U.K.

DOI:10.1109/JPHOT.2019.2927392

Manuscript received May 23, 2019; revised June 30, 2019; accepted July 3, 2019. Date of publication July 9, 2019; date of current version July 18, 2019. This work was supported in part by the National Natural Science Foundation of China under Grant 61875238, in part by the Beijing Youth Top-Notch Talent Support Program under Grant 2015000026833ZK08, in part by the Fund of State Key Laboratory of Information Photonics and Optical Communications (Beijing University of Posts and Telecommunications) P. R. China under Grant IPOC2017ZZ05, and in part by the Research Grant Council of Hong Kong under Grants PolyU152144/15E and PolyU152471/16E. Corresponding authors: Jinhui Yuan; Feng Li (e-mail: yuanjinhui81@bupt.edu.cn; enlf@polyu.edu.hk).

Abstract: Spectral compression (SPC) can be used for generating narrow bandwidth and wavelength-tunable light sources, which have important applications in optical communication system, spectroscopy, and nonlinear microscopy. In this paper, we numerically demonstrate the high-degree SPC of the chirp-free femtosecond pulse at wavelength 2.4 μm in a 6-cm long adiabatically suspended silicon waveguide taper. The silicon waveguide taper is designed with a dispersion-increasing profile along the propagation distance *z*. Simulation results show that the SPC factor can be up to 10.9, along with the brightness-enhanced factor of 8.0 and negligible sidelobe. The impacts of the higher order dispersion, higher order nonlinearity, losses (including linear and nonlinear loss), and variation of Kerr nonlinear coefficient along *z* on the SPC are also investigated. It is found that variation of Kerr nonlinear coefficient $\gamma(z)$ and linear loss are the dominant perturbation to the degradation of the SPC performance.

Index Terms: Spectral compression, soliton, suspended silicon waveguide taper.

1. Introduction

Coherent optical sources with narrow bandwidth and high spectral brightness are important in optical coherence tomography [1], [2], coherent anti-Stokes Raman scattering spectroscopy [3], [4], and all-optical analog-to-digital converter (AOADC) [5]–[7]. In the AOADC based on soliton self-frequency shift (SSFS), the quantization resolution is related to the amount of wavelength shift and spectrum width. Narrower spectral width is beneficial to higher quantization resolution [8]. Spectral compression (SPC) is one of the effective methods to obtain narrow spectral width. In

1978, the SPC was firstly reported in a single-mode optical fiber [9]. After then, the SPC has been demonstrated in a variety of optical fibers, such as optical gain fiber [10], [11], highly nonlinear fiber [12], and photonic crystal fiber [13], [14].

Recently, the SPCs with large compression factor and low sidelobe are achieved in dispersion-increasing fibers (DIFs). At present, linearly [15], [16], comb-profile [17], and exponentially [18] DIFs are developed. Lin *et al.* experimentally achieved the SPC of 102.8-fold in a 1-km long linearly DIF when the pre-chirped input pulses are used [15]. Such a high SPC factor is mainly induced by the SSFS, while the center wavelength of the input pulses is shifted. Nishizawa *et al.* obtained high-quality narrow spectrum with low sidelobe by utilizing the comb-profile DIF [17], [19]. The alignment and connection of the comb fibers increase the complexity and instability of the system. The SPCs of the chirp-free hyperbolic secant and Gaussian pulses were investigated in an exponentially DIF [18]. The optical fibers are used as the desired media for achieving the SPC. However, the length of optical fibers required is usually up to thousands of meters, which is not benefit to the development of on-chip laser sources. Besides, all the works are focused on the communication band. There are few works on the SPCs in the attractive mid-infrared (MIR) region since the propagation losses of the optical fibers are very high in the MIR region. Fortunately, as the CMOS technology matures gradually, the optical waveguides have been fabricated and applied in the on-chip devices and systems. Compared to the optical fibers, the optical waveguides have the unique characteristics of adjustable dispersion and high Kerr nonlinearity. Until now, there are few reports on utilizing the optical waveguide to fulfill the MIR SPC. In the previous works, we preliminarily demonstrated the SPCs in the uniform silicon nitride and chalcogenide waveguides, where the SPCs were resulted from self-phase modulation (SPM) [20], [21]. However, the spectral width is not monotonically decreased, and the waveguide length needs to be strictly controlled to obtain large compression factor. In addition, nonlinear indices of the silicon nitride and chalcogenide materials used are smaller, which greatly limits the process of the SPC. In contrast, the silicon material has large nonlinear index. Moreover, the nonlinear losses including two photon absorption (TPA) and free-carrier absorption (FCA) can be greatly reduced when pump pulse works in the spectral region beyond 2.2 μm [22], [23]. Therefore, it is possible to achieve the high-degree SPC at the MIR region in silicon waveguide.

In this paper, we numerically demonstrate the high-degree SPC of the chirp-free femtosecond pulse at wavelength 2.4 μm in a 6-cm long adiabatically suspended silicon waveguide taper, which is designed with a dispersion-increasing profile along the propagation distance. This paper is arranged as follows. In Section 2, the adiabatic theory of the SPC and modified generalized nonlinear Schrödinger equation (GNLSE) are introduced. In Section 3, adiabatically suspended silicon waveguide taper is designed for dispersion-increasing profile. The SPC results in the designed waveguide taper are demonstrated numerically in Section 4. We draw the conclusions in Section 5.

2. Theoretical Model

In the MIR region, the nonlinear propagation dynamics of short pulse inside a silicon waveguide taper can be described by the following GNLSE when the higher-order dispersion (HOD), higher-order nonlinearity (HON), variation of Kerr nonlinear coefficient, and losses are considered [24]–[26]

$$\frac{\partial A}{\partial z}+\frac{\alpha}{2}A-\sum_{k\geq 2}\frac{i^{k+1}}{k!}\beta_k(z)\frac{\partial^k A}{\partial T^k}=i\gamma(z)\left(1+i\tau_{shock}\frac{\partial}{\partial T}\right)|A|^2A-\frac{\gamma_{3PA}}{3A_{eff}^2(z)}|A|^4A, \tag{1}$$

where $A(z, t)$ is the envelope of slowly varying electric field in a co-propagation frame at the group-velocity $1/\beta_1$ along propagation distance z. T is the retarded time. α represents the linear loss, and $\beta_k(z)$ are the k-th ($k = 2$, 3, 4, 5, and 6) order dispersion coefficients at the central angular frequency ω_0 for different z. $\tau_{\text{shock}} = 1/\omega_0$ describes the self-steepening effect. $\gamma_{3\text{PA}}$ is the 3PA coefficient, which causes the nonlinear loss in the MIR region from 2.2 to 3.2 μm [23]. And γ is the

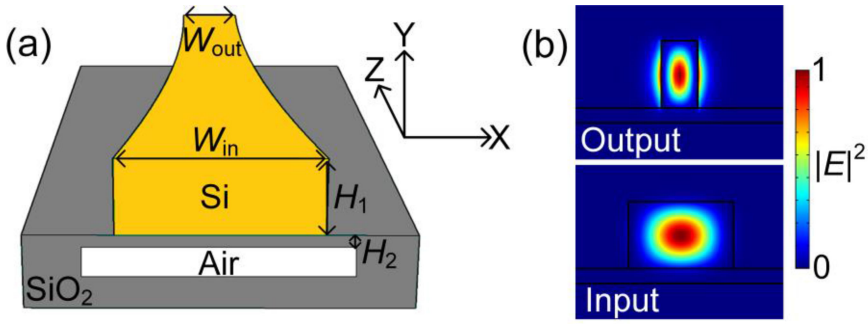

Fig. 1. (a) The three-dimensional schematic of the silicon waveguide taper designed. (b) Fundamental quasi-TE mode profiles calculated at the input and output ports of the waveguide taper when pump wavelength is located at 2400 nm.

nonlinear coefficient, which is defined as [27]

$$\gamma = \frac{\omega n_2(x, y)}{cA_{eff}}, A_{eff} = \frac{\left(\int\int_{-\infty}^{\infty} |F(x, y)|^2 dxdy\right)^2}{\int\int_{-\infty}^{\infty} |F(x, y)|^4 dxdy}, \tag{2}$$

where $n_2(x, y)$ represents the distribution of the Kerr nonlinear index, and $F(x, y)$ corresponds to the electric field distribution of the fundamental mode.

In order to explain the principle of the SPC in the dispersion-increasing waveguide, we can only consider the effects of group-velocity dispersion (GVD) and SPM on the short pulse. Therefore, the GNLSE can be modified as the NLSE

$$\frac{\partial A}{\partial z} = -\frac{i\beta_2(z)}{2}\frac{\partial^2 A}{\partial t^2} + i\gamma(z)|A|^2 A. \tag{3}$$

In the anomalous dispersion region, the soliton order N is given by [28]

$$N^2 = \frac{\frac{T^2(z)}{|\beta_2(z)|}}{\frac{1}{\gamma(z)P(z)}} = \gamma(z)[P(z)T(z)]\frac{T(z)}{|\beta_2(z)|}, \tag{4}$$

where $P(z)$ and $T(z)$ represent the peak power and pulse width, respectively, and the product of $P(z)T(z)$ represents the half of the energy of a hyperbolic secant pulse. The SPC principle can be explained by Eq. (4). Because of the energy conservation, the product of $P(z)T(z)$ keeps constant along z. When a chirp-free fundamental soliton pulse (transform-limited pulse) is injected into the dispersion-increasing waveguide, if the change of $\gamma(z)$ is smaller than $|\beta_2(z)|$, $T(z)$ will be broadened when $|\beta_2(z)|$ increases along z. N will eventually approach 1 because of soliton effect during the propagation. Because the perturbed fundamental soliton is gradually broadened while its temporal waveform remains unchanged, the corresponding optical spectrum will be compressed. This is a reverse operation of adiabatic temporal soliton compression [29]–[31]. If the change of $\gamma(z)$ is bigger than $|\beta_2(z)|$, the part of $\gamma/|\beta_2(z)|$ needs to be decreased to increase the value of $T(z)$ to fulfill the SPC. Thus, the value of $\gamma(z)$ needs to be reduced.

3. Design of Adiabatically Suspended Silicon Waveguide Taper

A suspended silicon waveguide taper is designed to ensure that optical field is well confined and short pulse changes adiabatically during propagation. Fig. 1(a) shows the three-dimensional schematic of the designed waveguide taper, where the rib height $H_1 = 900$ nm and membrane height $H_2 = 200$ nm. The rib width W varies adiabatically from 1400 to 490 nm, which obeys the

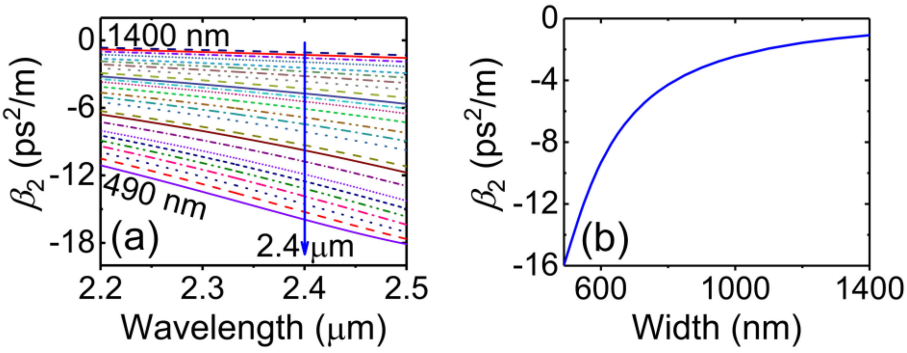

Fig. 2. (a) The GVD parameter β_2 of the silicon waveguide taper designed as a function of wavelength. The blue arrow indicates pump wavelength. (b) The relationship between β_2 and W at pump wavelength 2.4 μm.

following condition [30]

$$\frac{\lambda}{W}\frac{dW}{dz} \ll n_{\text{eff}} - 1. \tag{5}$$

where λ is the wavelength of short pulse and n_{eff} is the effective refractive index. The waveguide length L is set as 6 cm. Such a waveguide taper can be fabricated by the combination of deposition, etching, and bonding techniques [32], [33]. Fig. 1(b) shows the fundamental quasi-TE mode profiles calculated at the input ($z = 0$ cm) and output ($z = 6$ cm) ports of the waveguide when pump wavelength is located at 2400 nm. From Fig. 1(b), the mode field is well confined in the core region of silicon waveguide taper especially at the input port. At the output port, the mode field begins to leak into the air cladding, while the mode field energy leaked into the membrane can be ignored. Except for the fundamental mode, other modes are also propagated inside the waveguide. As W decreases, the number of the quasi-TE mode also decreases from 11 to 2. These modes have different linear and nonlinear characteristics. To avoid the mode coupling resulted from the tight confinement, the offset pumping technique can be used to only excite the fundamental mode [34].

With the finite element method, we calculate the GVD parameter β_2 under different W, as shown in Fig. 2(a). From Fig. 2(a), the absolute value $|\beta_2|$ is larger for smaller W. With the increase of wavelength, the difference between β_2 for different W gradually becomes larger. The main reason is considered that dispersion of waveguide taper is determined by W and the restrain ability of optical field for smaller W becomes weak. In this work, the pump wavelength is chosen as 2.4 μm, as indicated by the blue arrow in Fig. 2(a). The relationship between β_2 and W at pump wavelength 2.4 μm is shown in Fig. 2(b). It can be seen from Fig. 2(b) that $|\beta_2|$ increases monotonically from 1.08 to 15.93 ps^2/m when W varies from 1400 to 490 nm.

The variation of W versus z is plotted in Fig. 3(a). The decrement of $W(z)$ gradually slows down along z. The relationship between β_2 and z is also shown in Fig. 3(a). The linearly increasing dispersion profile is fulfilled as following

$$\beta_2(z) = \beta_2(0) + \frac{\beta_2(L) - \beta_2(0)}{L} z, \tag{6}$$

where $\beta_2(0)$ and $\beta_2(L)$ are the dispersion values at the input and output posts of the waveguide taper, respectively. Fig. 3(b) shows the variations of $\gamma(z)$ and $A_{\text{eff}}(z)$ along z. From Fig. 3(b), the variations of $\gamma(z)$ and $A_{\text{eff}}(z)$ are not monotonic. $\gamma(z)$ first increases quickly to the maximum value and then decreases monotonically to the minimum value at the output port. The ratio between the maximum and minimum values of $\gamma(z)$ is 1.66, which is much smaller than that of dispersion (14.75). In contrast, the variation of $A_{\text{eff}}(z)$ appears an opposite trend.

Generally speaking, during the design and optimization process of waveguides and other nanophotonics, non-uniqueness of the desired solution is one of the main challenges. Typically,

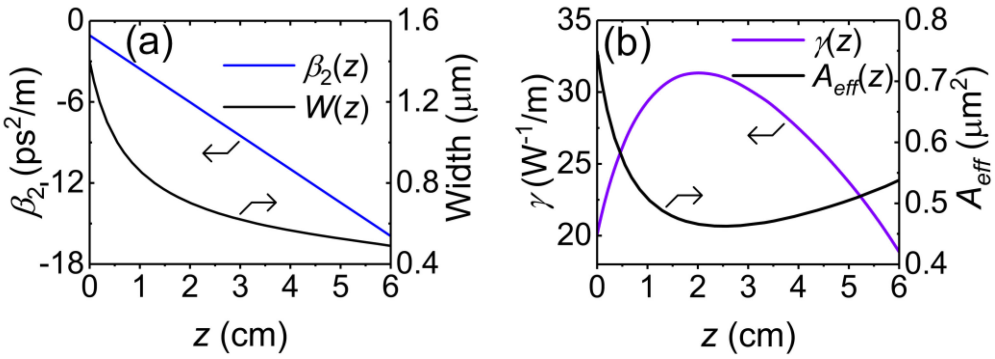

Fig. 3. (a) The variations of β_2 (blue solid line) and W (black solid line) along z, and (b) the variations of γ (blue solid line) and A_{eff} (black solid line) along z.

the desired response can be obtained from multiple sets of design parameters and this cause convergence issues for conventional inverse design approaches. Recently, lots of interest has been paid to overcoming the non-uniqueness challenge. Central to these efforts are introducing pseudo-encoder to encounter this challenge. The method relies on reducing the dimensionality of both design and response space and turns the ill-posed many to one inverse problem to a one-to-one problem [35], [36]. Moreover, generative neural networks have been introduced as effective optimization techniques to optimize a certain class of nanostructures [37], [38].

4. The SPC of the Femtosecond Pulse

Eq. (1) is calculated by using the Runge-Kutta method [39]. A chirp-free hyperbolic secant pulse with full width at half maximum (FWHM) of 50 fs at 2.4 μm is launched into the designed waveguide taper. $\beta_2(0)$ and $\gamma(0)$ are -1.08 ps^2/m and 20.09 W^{-1}/m, respectively. The input peak power P_0 is assumed to be 66.64 W so as to guarantee $N = 1$. Here, α and γ_{3PA} are set as 0.274 dB/cm [40] and 0.0012 cm^3/GW^2 [41], respectively. Figs. 4(a) and 4(b) show the evolutions of the spectral and temporal profiles along z. From Figs. 4(a) and 4(b), although some sidelobes appear at the initial stage, they are obviously suppressed at the end of propagation. The optical spectrum is evidently compressed during the propagation, along with the increasing peak power. The pulse width monotonously increases from 50 to 749 fs accompanying with the reduction of the peak power. In Fig. 4(c), the spectral shift cannot be clearly seen. However, it can be seen from Fig. 4(d) that the peak position of the temporal pulse is right shifted about 280 fs. When the impacts of HOD, HON, variation of $\gamma(z)$, and losses are neglected, the outputs in the ideal case (NLSE) are also given in Figs. 4(c) and 4(d). Low-level sidelobes are symmetrically generated on both sides of the optical spectrum, which are resulted from the four-wave mixing (FWM) [42]. The sidelobe level is calculated as -16 dB.

The spectral compression factor (SCF) and brightness-enhanced factor (BEF) are introduced to evaluate the quality of the SPC, which are defined as

$$\mathrm{SCF} = \mathrm{BW}_{\mathrm{FWHM\_in}}/\mathrm{BW}_{\mathrm{FWHM\_out}}, \mathrm{BEF} = \mathrm{P}_{\mathrm{Spectrum\_out}}/\mathrm{P}_{\mathrm{Spectrum\_in}}, \tag{7}$$

where $BW_{\mathrm{FWHM\_in}}$ and $BW_{\mathrm{FWHM\_out}}$ are the spectral bandwidths at the input and output ports, and $P_{\mathrm{Spectrum\_in}}$ and $P_{\mathrm{Spectrum\_out}}$ are the spectral peak powers at the input and output ports. Fig. 5(a) shows the variations of spectral bandwidth and peak power along z. From Fig. 5(a), BW_{FWHM} is reduced monotonously from 121.0 to 11.1 nm, and spectral peak power is enhanced by 8.0 times. The variations of the SCF and BEF versus z are plotted in Fig. 5(b). At the output port, the SCF and BEF can be up to 10.9 and 8.0, respectively.

To clearly understand the physical mechanism of the SPC, the impacts of the HOD, HON, losses, and variation of $\gamma(z)$ on the SPC are investigated. Fig. 6 shows the evolutions of BW_{FWHM} and peak

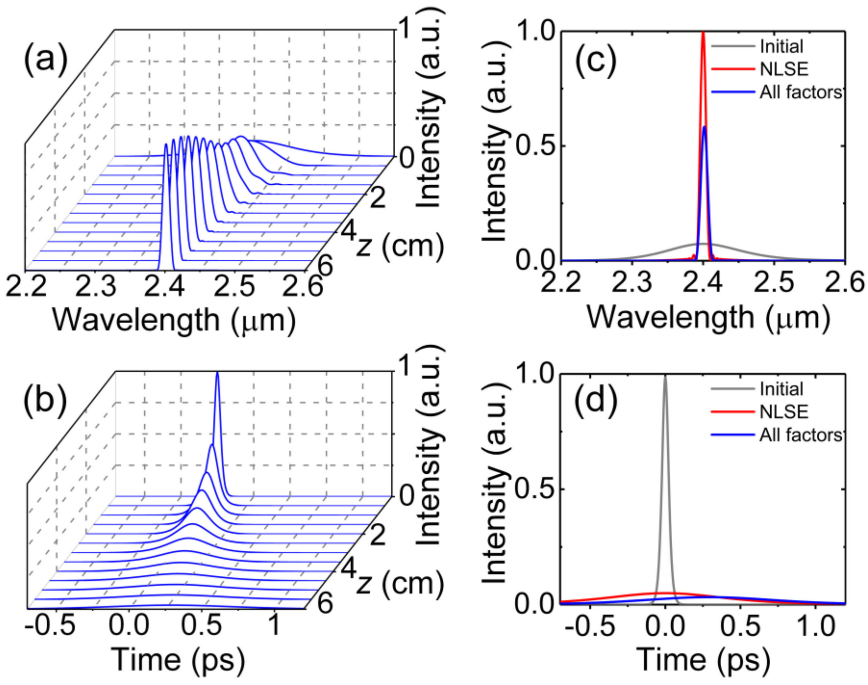

Fig. 4. The evolutions of (a) spectral and (b) temporal profiles along z modeled by Eq. (1). The normalized outputs of (c) spectral and (d) temporal profiles (blue lines). The initial profiles (gray lines) and the outputs in the ideal case (NLSE) (red lines) are also plotted for comparison.

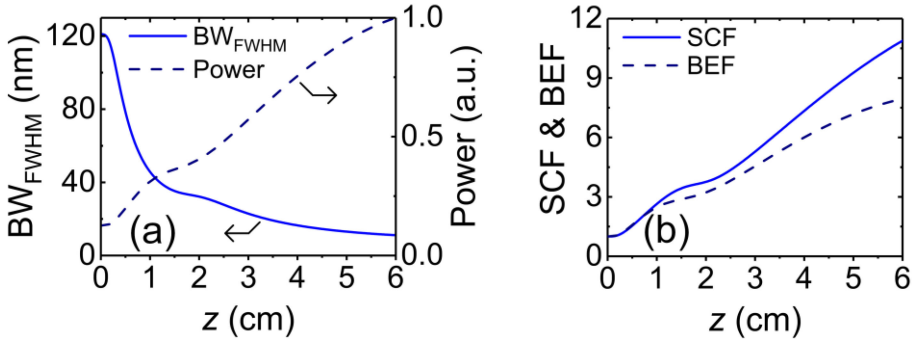

Fig. 5. (a) The evolutions of spectral bandwidth (solid line) and peak power (dash line) as functions of z. (b) The variation of spectral compression factor (SCF) (solid line) and brightness-enhanced factor (BEF) (dash line) along z.

power under different cases. The cases of the NLSE and all factors are also plotted for comparison. From Fig. 6, BW_{FWHM} shows an exponential decreasing trend while spectral peak power shows a linear increasing trend. The curves of the HOD and HON are overlapped with that of the NLSE. The curve of $\gamma(z)$ shows the maximum deviation from the NLSE in both BW_{FWHM} and peak power. The curve of the losses coincides with the NLSE for BW_{FWHM} at the beginning stage, and then deviates from the NLSE. Its power curve is much lower than the NLSE. The SCF and BEF values are listed in Table 1. It can be seen from Table 1 that variation of $\gamma(z)$ and losses have the largest impact on the SPC. The impacts of the HOD and HON can be ignored.

Figures. 7(a) and 7(b) show the output spectral and temporal waveforms when the HOD, HON, losses, and variation of $\gamma(z)$ are considered. From Figs. 7(a) and 7(b), the waveform of the HOD agrees well with that of the NLSE both in spectral and temporal domains. For the HON, the center

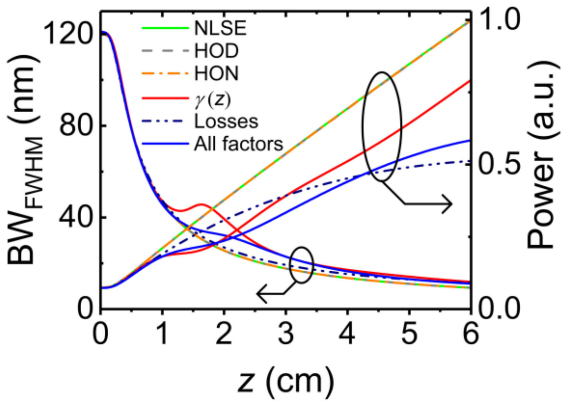

Fig. 6. The evolutions of BW_{FWHM} and peak power along z when the HOD (gray dash lines), HON (orange dash dot lines), $\gamma(z)$ (red solid lines), and losses (navy dash dot dot lines) are considered, respectively. The cases for the NLSE (green solid lines) and all factors (blue solid lines) are also plotted for comparison.

TABLE 1
The SCF and BEF Values Obtained for Different Cases

Cases	SCF	BEF
NLSE	12.98	13.62
HOD	12.98	13.60
HON	12.98	13.61
γ(z)	10.18	10.79
Losses	10.65	6.98
All factors	10.88	7.95

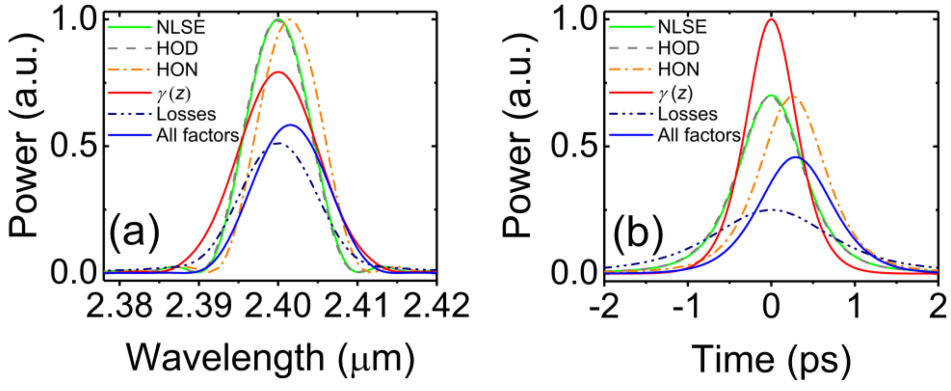

Fig. 7. The outputs of (a) spectral and (b) temporal waveforms when the HOD (gray dash lines), HON (orange dash dot lines), $\gamma(z)$ (red solid lines), and losses (navy dash dot dot lines) are considered. The NLSE (green solid lines) and all factors (blue solid lines) are also plotted for comparison.

wavelength is slightly red-shifted, and the waveform is delayed by a few femtoseconds. Sidelobe appears at both sides of spectrum for the HOD, HON. However, for variation of $\gamma(z)$ and losses, the sidelobe disappears and spectral peak power drops a lot.

From the above analyses, the effect of the HOD on the SPC can be ignored. In order to explain the reason quantitatively, the dispersion length L_{Dk} ($k = 2, 3, 4, 5$, and 6), which describes the effect

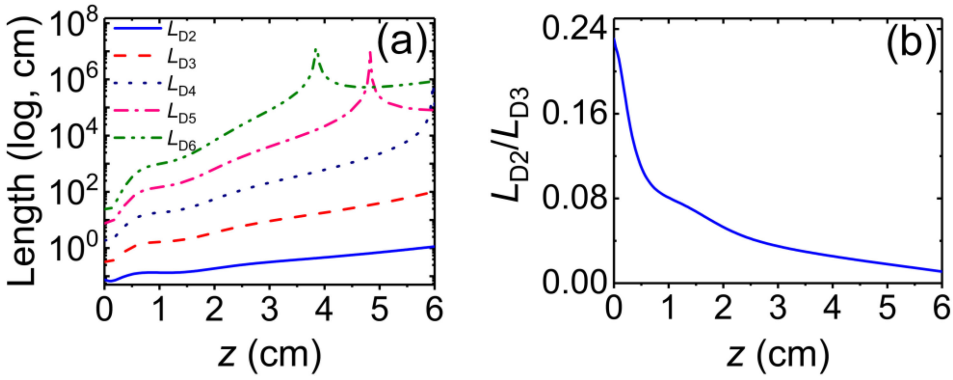

Fig. 8. The evolutions of (a) dispersion lengths L_{D2} (blue solid line), L_{D3} (red dash line), L_{D4} (navy dot line), L_{D5} (pink dash line), and L_{D6} (olive dash dot dot line) in the logarithmic scales, and (b) the ratio between L_{D2} and L_{D3} along z.

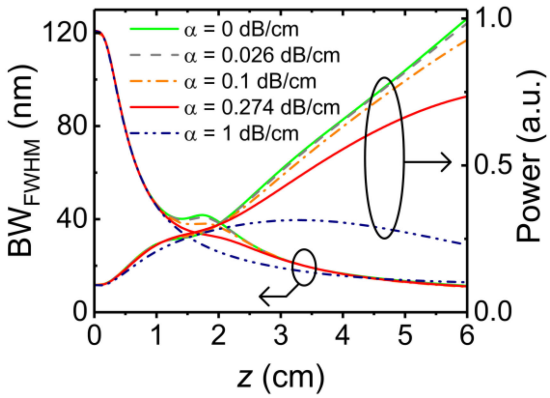

Fig. 9. The evolutions of BWFWHM and peak power along z for $\alpha = 0.026$ (gray dash lines), 0.1 (orange dash dot lines), 0.274 (red solid lines), and 1 dB/cm (navy dash dot dot lines). The case of $\alpha = 0$ dB/cm (green solid lines) is also plotted for comparison.

of k-th dispersion, is introduced. L_{Dk} is defined as

$$L_{Dk}(z) = \frac{T_0^k(z)}{|\beta_k(z)|}, \tag{8}$$

where $T_0(z)$ is the pulse width at z. As seen from Fig. 8(a), L_{D2}, L_{D3}, and L_{D4} increase monotonously along z. L_{D5} and L_{D6} first increase and then decrease. All L_{Dk} ($k > 3$) are much larger than L_{D2}, which indicates that the effect of the HOD is much weaker than β_2. Fig. 8(b) shows the ratio between L_{D2} and L_{D3}. The maximum value of L_{D2}/L_{D3} is less than 0.24 and reduces continuously along z. Thus, compared with β_2, the effect of β_3 is very weak.

The roughness of the waveguide sidewall is the main loss factor. At present, with some advanced fabrication methods [40], [43], [44], α can be reduced to 0.026 dB/cm. In order to make the silicon waveguide taper more practical, some typical values of α are used in our simulation when all factors are considered, as shown in Fig. 9. The evolutions of BW_{FWHM} and peak power along z are demonstrated. The case of $\alpha = 0$ dB/cm is also plotted for comparison. The corresponding SCF and BEF values under different α are given in Table 2.

In Fig. 9, the curves of BW_{FWHM} for different α start to separate near $z = 1$ cm and meet at $z = 4$ cm. The corresponding curves of spectral peak power separate at $z = 2$ cm. In Table 2, the SCF and BEF values are almost equivalent up to $\alpha = 0.1$ dB/cm. The difference between them gradually

TABLE 2
The SCF and BEF Values Obtained Under Different α

α (dB/cm)	SCF	BEF
0	10.67	10.81
0.026	10.83	10.64
0.1	11.08	10.03
0.274	10.88	7.95
1	9.38	2.48

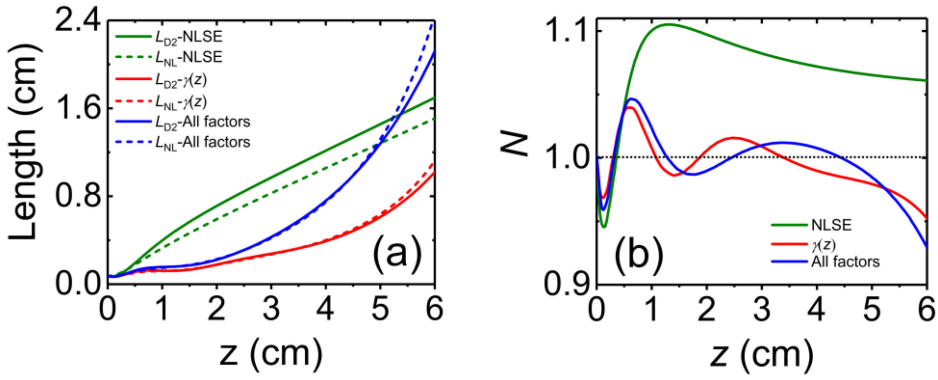

Fig. 10. (a) The evolutions of L_{D2} (solid lines), L_{NL} (dash lines), and (b) the soliton order N along z under the cases of NLSE (olive lines), variation of $\gamma(z)$ (red lines), and all factors (blue lines). The black dot curve in (b) corresponds to the fundamental soliton ($N = 1$).

increases when α increases. It can be seen from Table 2 that α has little influence on the SCF while its impact on the BEF is significant. For larger α, the deviation between the ideal adiabatic case and practical case is large. Thus, the smaller α is beneficial for the SCF and BEF.

Finally, we will investigate the variation of $\gamma(z)$, which has a significant impact on the SPC. The impact of variation of $\gamma(z)$ can be evaluated by nonlinear length L_{NL}, which is defined as

$$L_{NL}(z) = \frac{1}{\gamma(z)P(z)}, \tag{9}$$

where $P(z)$ is the temporal peak power along z. It is known that the HOD and HON have small effects on the SCF. Thus, the three cases of the NLSE, $\gamma(z)$, and all effects are considered. Fig. 10(a) shows the evolutions of L_{D2} and L_{NL} along z under the three cases. As seen from Fig. 10(a), the difference between L_{D2} and L_{NL} is very small, except for the case of the NLSE. Besides, the values of L_{NL} and L_{D2} are smaller within the length of the waveguide taper, which means that the dispersion and nonlinear effect will jointly play a significant role during propagation. For the case of NLSE, the variation of $\gamma(z)$ is a constant, so the value of L_{NL} is smaller L_{D2} after $z = 0.5$ cm. It means that the nonlinearity is slightly larger than the dispersion. Some sidelobes appear due to the FWM, as seen from Figs. 4 and 7. The appearances of sidelobes can enhance the SPC at the expense of quality of spectral swings. For a waveguide taper designed with specific dispersion profile, it is difficult to maintain the nonlinearity as a constant. For the cases of $\gamma(z)$ and all factors, the variation of $\gamma(z)$ first increases and then decreases, and the values of L_{NL} and L_{D2} are nearly equivalent except for that at the output end. It means that the nonlinearity effect is slightly smaller than the dispersion. The FWM effect becomes weak and sidelobes nearly disappear, as seen from Figs. 4 and 7. The SCF and BEF values are reduced compared to the case of NLSE. Soliton order $N^2 = L_{D2}/L_{NL}$ under the three cases are also plotted in Fig. 10(b) so as to investigate the evolution of N along z. The evolution of N can also make us observe the tiny difference between

L_{NL} and L_{D2} shown in Fig. 10(a). In Fig. 10(b), the dot line corresponds to $N = 1$, which represents the fundamental soliton. From Fig. 10(b), the value of N occurs to oscillate between 0.946 and 1.105 for the case of NLSE, 0.968 and 1.040 for the case of $\gamma(z)$, and 0.958 and 1.047 for the case of all factors. It indicates that the temporal pulses under the three cases are propagated in the form of the fundamental soliton.

5. Conclusion

In summary, we propose an adiabatically suspended silicon waveguide taper to achieve the SPC at the mid-infrared spectral region. The silicon waveguide taper is designed with a dispersion-increasing profile along z. With the designed waveguide taper, the optical spectrum of the chirp-free femtosecond pulse is efficiently compressed. The SCF can be up to 10.9, along with the BEF of 8.0 and negligible sidelobe after the 6-cm propagation. By considering the impacts of the HOD, HON, losses (including linear and nonlinear loss), and variation of $\gamma(z)$ on the SPC, it is found that variation of $\gamma(z)$ and linear loss are the dominant perturbation to the degradation of the SPC performance. It is believed that the proposed SPC scheme paves the way for obtaining the integrated mid-infrared light sources with narrow spectral width, which can find important applications in developing the on-chip optoelectronic devices and systems.

References

[1] R. Huber, M. Wojtkowski, and J. G. Fujimoto, "Fourier domain mode locking (FDML): A new laser operating regime and applications for optical coherence tomography," *Opt. Exp.*, vol. 14, no. 8, pp. 3225–3237, 2006.

[2] I. Grulkowski *et al.*, "Retinal, anterior segment and full eye imaging using ultrahigh speed swept source OCT with vertical-cavity surface emitting lasers," *Biomed. Opt. Exp.*, vol. 3, no. 11, pp. 2733–2751, 2012.

[3] E. R. Andresen, V. Birkedal, J. Thøgersen, and S. R. Keiding, "Tunable light source for coherent anti-Stokes Raman scattering microspectroscopy based on the soliton self-frequency shift," *Opt. Lett.*, vol. 31, no. 9, pp. 1328–1330, 2006.

[4] M. Marangoni, A. Gambetta, C. Manzoni, V. Kumar, R. Ramponi, and G. Cerullo, "Fiber-format CARS spectroscopy by spectral compression of femtosecond pulses from a single laser oscillator," *Opt. Lett.*, vol. 34, no. 21, pp. 3262–3264, 2009.

[5] T. Nishitani, T. Konishi, and K. Itoh, "Resolution improvement of all-optical analog-to-digital conversion employing self-frequency shift and self-phase modulation induced spectral compression," *IEEE J. Sel. Topics Quantum Electron.*, vol. 14, no. 3, pp. 724–732, May/Jun. 2008.

[6] Z. Kang *et al.*, "Six-bit all-optical quantization using photonic crystal fiber with soliton self-frequency shift and pre-chirp spectral compression techniques," *Chin. Phys. B*, vol. 22, no. 11, 2013, Art. no. 114211.

[7] X. Kang *et al.*, "Integratable all-optical spectral quantization scheme based on chalcogenide-silicon slot waveguide," *Opt. Commun.*, vol. 355, pp. 479–484, 2015.

[8] T. Konishi, K. Tanimura, K. Asano, Y. Oshita, and Y. Ichioka, "All-optical analog-to-digital converter by use of self-frequency shifting in fiber and a pulse-shaping technique," *J. Opt. Soc. Amer. B*, vol. 19, no. 11, pp. 2817–2823, 2002.

[9] R. H. Stolen and Chinlon Lin, "Self-phase-modulation in silica optical fibers," *Phys. Rev. A*, vol. 17, no. 4, pp. 1448–1453, 1978.

[10] J. Limpert *et al.*, "High-power picosecond fiber amplifier based on nonlinear spectral compression," *Opt. Lett.*, vol. 30, no. 7, pp. 714–716, 2005.

[11] J. Limpert, T. Gabler, A. Liem, H. Zellmer, and A. Tünnermann, "SPM-induced spectral compression of picosecond pulses in a single-mode Yb-doped fiber amplifier," *Appl. Phys. B*, vol. 74, no. 2, pp. 191–195, 2002.

[12] H. P. Li *et al.*, "Soliton self-frequency shift and spectral compression in highly nonlinear fibers for resolution improvement of all-optical analogue-to-digital conversion," *Electron. Lett.*, vol. 45, no. 25, pp. 1337–1339, 2009.

[13] E. R. Andresen, J. Thøgersen J, and S. R. Keiding, "Spectral compression of femtosecond pulses in photonic crystal fibers," *Opt. Lett.*, vol. 30, no. 15, pp. 2025–2027, 2005.

[14] E. R. Andresen, J. M. Dudley, D. Oron, C. Finot, and H. Rigneault, "Transform-limited spectral compression by self-phase modulation of amplitude-shaped pulses with negative chirp," *Opt. Lett.*, vol. 36, no. 5, pp. 707–709, 2011.

[15] Y.-S. Lin and C.-B. Huang, "Large-scale and structure-tunable laser spectral compression in an optical dispersion-increasing fiber," *Opt. Exp.*, vol. 25, no. 15, pp. 18024–18030, 2017.

[16] W. T. Chao, Y. Y. Lin, J. L. Peng, and C. B. Huang, "Adiabatic pulse propagation in a dispersion-increasing fiber for spectral compression exceeding the fiber dispersion ratio limitation," *Opt. Lett.*, vol. 39, no. 4, pp. 853–856, 2014.

[17] N. Nishizawa, K. Takahashi, Y. Ozeki, and K. Itoh, "Wideband spectral compression of wavelength-tunable ultrashort soliton pulse using comb-profile fiber," *Opt. Exp.*, vol. 18, no. 11, pp. 11700–11706, 2010.

[18] Q. Li, T. W. Zhang, and M. F. Li, "Spectral compression of chirp-free optical pulses in fibers with exponentially increasing dispersion," *J. Opt. Soc. Amer. B*, vol. 34, no. 9, pp. 1796–1804, 2017.

[19] N. Nishizawa, Y. Andou, E. Omoda, H. Kataura, and Y. Sakakibara, "Characteristics and improvement of wideband wavelength-tunable narrow-linewidth source by spectral compression in quasi-dispersion-increasing comb-profile fiber," *Opt. Exp.*, vol. 24, no. 20, pp. 23403–23418, 2016.
[20] C. Mei, J. H. Yuan, K. R. Wang, X. Z. Sang, and C. X. Yu, "Chirp-free spectral compression of parabolic pulses in silicon nitride channel waveguides," in *Proc. OptoElectron. Commun. Conf.*, Niigata, Japan, 2016, pp. 1–3.
[21] Z. L. Li *et al.*, "Mid-infrared spectral compression of parabolic pulses in a chalcogenide ridge waveguide," in *Proc. Conf. Lasers Electro-Opt. Pac. Rim, CLEO-PR*, Hong Kong, China, 2018, pp. 1–2.
[22] L. Zhang, A. M. Agarwal, L. C. Kimerling, and J. Michel, "Nonlinear group IV photonics based on silicon and germanium: From near-infrared to mid-infrared," *Nanophotonics*, vol. 3, no. 4/5, pp. 247–268, 2014.
[23] Z. L. Wang, H. J. Liu, N. Huang, Q. B. Sun, J. Wen, and X. F. Li, "Influence of three-photon absorption on mid-infrared cross-phase modulation in silicon-on-sapphire waveguides," *Opt. Exp.*, vol. 21, no. 2, pp. 1840–1848, 2013.
[24] R. K. W. Lau, M. R. E. Lamont, A. G. Griffith, Y. Okawachi, M. Lipson, and A. L. Gaeta, "Octave-spanning mid-infrared supercontinuum generation in silicon nanowaveguides," *Opt. Lett.*, vol. 39, no. 15, pp. 4518–4521, 2014.
[25] N. Singh *et al.*, "Midinfrared supercontinuum generation from 2 to 6 μm in a silicon nanowire," *Optica*, vol. 2, no. 9, pp. 797–802, 2015.
[26] Z. Q. Wang, L. Shi, X. B. Xu, J. H. Zhang, J. L. Zhang, and X. L. Zhang, "Optical nonreciprocity with large bandwidth in asymmetric hybrid slot waveguide coupler," *Opt. Exp.*, vol. 23, no. 3, pp. 3690–3698, 2015.
[27] G. P. Agrawal, "Chapter 2 pulse propagation in fibers," *in Nonlinear Fiber Optics*, 4th ed. San Francisco, CA, USA: Academic, pp. 25–50, 2009.
[28] R. Liang, X. J. Zhou, Z. Y. Zhang, Z. J. Qin, H. P. Li, and Y. Liu, "Numerical investigation on spectral compression of femtosecond soliton in a dispersion-increasing fiber," *Opt. Fiber Technol.*, vol. 15, no. 5/6, pp. 438–441, 2009.
[29] K. R. Tamura and M. Nakazawa , "54-fs, 10-GHz soliton generation from a polarization-maintaining dispersion-flattened dispersion-decreasing fiber pulse compressor," *Opt. Lett.*, vol. 26, no. 11, pp. 762–764, 2001.
[30] S. Lavdas, J. B. Driscoll, R. R. Grote, R. M. Osgood, and N. C. Panoiu, "Pulse compression in adiabatically tapered silicon photonic wires," *Opt. Exp.*, vol. 22, no. 6, pp. 6296–6312, 2014.
[31] J. C. Travers *et al.*, "Optical pulse compression in dispersion decreasing photonic crystal fiber," *Opt. Exp.*, vol. 15, no. 20, pp. 13203–13211, 2007.
[32] J. Chiles, S. Khan, J. C. Ma, and S. Fathpour, "High-contrast, all-silicon waveguiding platform for ultra-broadband mid-infrared photonics," *Appl. Phys. Lett.*, vol. 103, no. 15, 2013, Art. no. 151106.
[33] D. Y. Oh, K. Y. Yang, C. Fredrick, G. Ycas, S. A. Diddams, and K. J. Vahala, "Coherent ultra-violet to near-infrared generation in silica ridge waveguides," *Nature Commun.*, vol. 8, 2017, Art. no. 13922.
[34] R. Cherif, M. Zghal, L. Tartara, and V. Degiorgio, "Supercontinuum generation by higher-order mode excitation in a photonic crystal fiber," *Opt. Exp.*, vol. 16, no. 3, pp. 2147–2152, 2008.
[35] Y. Kiarashinejad, S. Abdollahrameazni, and A. Adibi, "Deep learning approach based on dimensionality reduction for designing electromagnetic nanostructures," 2019, *arXiv:1902.03865*.
[36] Y. Kiarashinejad, S. Abdollahrameazni, M. Zandehshahvar, O. Hemmatyar, and A. Adibi, "Deep learning reveals underlying physics of light-matter interactions in nanophotonic devices," 2019, *arXiv:1905.06889*.
[37] J. Q. Jiang and J. A. Fan, "Global optimization of dielectric metasurfaces using a physics-driven neural network," 2019, *arXiv:1906.04157*.
[38] J. Q. Jiang and J. A. Fan, "Dataless training of generative models for the inverse design of metasurfaces," 2019, *arXiv:1906.07843*.
[39] J. Hult, "A fourth-order Runge-Kutta in the interaction picture method for simulating supercontinuum generation in optical fibers," *J. Lightw. Technol.*, vol. 25, no. 12, pp. 3770–3775, Dec. 2007.
[40] P. Dong *et al.*, "Low loss shallow-ridge silicon waveguides," *Opt. Exp.*, vol. 18, no. 14, pp. 14474–14479, 2010.
[41] T. Wang *et al.*, "Multi-photon absorption and third-order nonlinearity in silicon at mid-infrared wavelengths," *Opt. Exp.*, vol. 21, no. 26, pp. 32192–32198, 2013.
[42] H. P. Li, X. J. Zhang, J. K. Liao, X. G. Tang, Y. Liu, and Y. Z. Liu, "Spectral compression of femtosecond pulses in photonic crystal fiber with anomalous dispersion," in *Proc. Asia Commun. Photon. Conf.*, Shanghai, China, 2009, pp. 1–2.
[43] M. Borselli, T. J. Johnson, and O. Painter, "Beyond the Rayleigh scattering limit in high-Q silicon microdisks: Theory and experiment," *Opt. Exp.*, vol. 13, no. 5, pp. 1515–1530, 2005.
[44] G. L. Li *et al.*, "Ultralow-loss, high-density SOI optical waveguide routing for macrochip interconnects," *Opt. Exp.*, vol. 20, no. 11, pp. 12035–12039, 2012.